RSC Advances

PAPER

View Article Online
View Journal | View Issue

Cite this: *RSC Adv.*, 2026, **16**, 4214

Sorbitol-modified graphene oxide-iron oxide nanocomposite for efficient doxycycline removal: mechanistic and kinetic insights

Afia Murshida Kusum, [ac] Md Humayun Kabir, [*b] Md. Safiqul Islam,[c] Md Sakil [ac] and Sabina Yasmin [*a]

This study reports the synthesis of a novel, eco-friendly and highly effective sorbitol-functionalized graphene oxide-iron oxide (GO/Fe-SBT) nanocomposite for the enhanced removal of doxycycline (DOX) from aqueous solutions. Comprehensive characterization (FTIR, XRD, SEM, TEM, and EDX) confirmed the successful incorporation of iron oxide nanoparticles and sorbitol into the GO matrix, leading to enhanced stability and dispersion as well as abundant active sites. The GO/Fe-SBT nanocomposite exhibited exceptional adsorption performance, achieving a maximum DOX removal efficiency of 96.82% within 5 minutes at an initial concentration of 0.2 mg L^{-1}. The equilibrium capacity reached 41.61 mg g^{-1} under optimal conditions (pH 5, adsorbent dosage of 0.1 g L^{-1}, temperature of 25 °C). The adsorption process followed pseudo-second-order kinetics and the Freundlich isotherm model, indicating chemisorption-dominated multilayer adsorption. The high removal efficiency was attributed to synergistic mechanisms, including electrostatic interactions, hydrogen bonding, π–π stacking and iron chelation. Moreover, the nanocomposite demonstrated excellent reusability, maintaining over 94% of its initial removal efficiency after seven consecutive adsorption–desorption cycles. Overall, this work introduces a rapid, low-dose, sustainable and highly effective adsorbent with strong potential for scalable mitigation of antibiotic contamination in aqueous environments.

Received 25th September 2025
Accepted 12th January 2026

DOI: 10.1039/d5ra07287e

rsc.li/rsc-advances

1. Introduction

Antibiotics have been widely used to treat infections in humans and animals because of their effective antimicrobial action and minimal side effects.[1–3] However, traces of these antibiotics are often found in soil, surface water, groundwater and even drinking water and are now recognized as a new category of global contaminants. In particular, the use of tetracycline antibiotics (TCs), a widely used class of antibiotics, has raised significant concern in recent years.[3–5] Doxycycline (DOX), a member of the tetracycline class, is extensively used in both human and veterinary medicine. This antibiotic remains effective against numerous bacteria, including both Gram-positive and Gram-negative.[6] Despite its broad usage and proven effectiveness, the environmental presence of DOX has become a significant concern. When DOX contaminates natural ecosystems, it may increase the growth and dispersal of resistant microorganisms, thereby endangering public health.[7] Consequently, the imperative is to remediate DOX from affected environments to mitigate its detrimental effects on ecological systems and the health of the population. However, removing DOX from wastewater is challenging for conventional treatments because of its stable chemical structure and nonbiodegradable nature.[8]

A variety of methods can be employed to eliminate DOX from water, including electrocoagulation,[9,10] ozonation,[11] electroflotation,[9,12] constructed wetlands,[13] photocatalytic degradation,[14,15] Fenton degradation,[16,17] and adsorption.[18] Among these methods, adsorption is a particularly popular choice because of its cost-effectiveness and high efficiency.[19,20] Researchers have explored the adsorption and removal of DOX using various materials, such as cationic resins,[21] chitosan particles,[22] aluminum oxide, activated carbon, single-walled and multi-walled carbon nanotubes,[23] biodegradable sorbents,[24] covalent organic framework-based membranes,[25] graphene as representative two-dimensional (2D) carbon materials,[26,27] and graphene-based nanomaterials.[28] While adsorption offers advantages in removing antibiotics, the process is often expensive and time intensive because most adsorptive materials have limited efficiency and are difficult to regenerate.[29] To overcome these limitations, developing a low-cost, high-efficiency, and reusable adsorptive material is crucial.

[a]*Institute of National Analytical Research and Service (INARS), Bangladesh Council of Scientific and Industrial Research (BCSIR), Dhanmondi, Dhaka-1205, Bangladesh. E-mail: sabinayasmin@bcsir.gov.bd*

[b]*Institute of Food Science and Technology (IFST), Bangladesh Council of Scientific and Industrial Research (BCSIR), Dhanmondi, Dhaka-1205, Bangladesh. E-mail: humayunkabir@bcsir.gov.bd*

[c]*Department of Chemistry, University of Dhaka, Dhaka-1000, Bangladesh*

Graphene oxide (GO)-based nanocomposites stand out as excellent candidates because of their superior ability to remove antibiotics.[30–32] GO contains abundant oxygen-bearing functional moieties (hydroxyl, carbonyl, carboxyl, and epoxide) distributed on its surface and edges.[30,33,34] It has an extensive surface area along with a planar configuration enriched with π-electrons.[34–36] Owing to its remarkable physical and chemical properties, GO has gained significant attention across diverse research fields.[37] However, pristine graphite and GO remain expensive, and their worldwide accessibility is relatively limited.[38] This challenge can be overcome by producing GO from electronic waste, particularly discarded dry-cell batteries. In our previous work, we successfully demonstrated the synthesis of GO from the graphite electrodes of used dry-cell batteries.[30,33,39,40] These waste graphite electrodes serve as a promising and sustainable precursor for GO synthesis, offering a dual benefit of cost reduction and effective electronic waste management.

The efficiency of GO can be enhanced through the incorporation of different metal and organic materials.[41] Metals such as Fe, Zn, TiO_2, and Au are commonly used to increase the efficiency of GO. Among these materials, Fe is particularly special because of its nontoxic nature and its ability to easily combine with other materials, such as carbon frameworks, activated carbon, and graphene. It enhances the biocompatibility, stability, and adsorption capacity of the composite. Fe ions act as coordination centers, forming stable chelate complexes with the oxygen and nitrogen donor groups of DOX (–OH, $–NH_2$, –C═O). This chelation, together with hydrogen bonding and electrostatic interactions, strengthens DOX binding to the composite surface, significantly improving its removal efficiency.[42] Sorbitol, a naturally occurring sugar alcohol, is an excellent organic modifier for enhancing the performance of GO. It contains multiple hydroxyl (–OH) groups, which can strongly interact with the oxygen-containing functional groups on GO *via* hydrogen bonding, leading to better dispersion and stability of GO sheets in aqueous media. Therefore, functionalizing GO with sorbitol enhances hydrophilicity and hydrogen-bonding sites, promoting efficient DOX adsorption and composite stability while maintaining eco-friendly, low-cost attributes.[43] To the best of our knowledge, no prior study has reported the synthesis of GO/Fe-SBT nanocomposite for the adsorption of antibiotics from wastewater.

The present study aims to develop and evaluate a novel, eco-friendly and highly effective GO/Fe-SBT nanocomposite for the efficient removal of DOX from aqueous solutions. The synthesized material was characterized *via* X-ray diffraction (XRD), Fourier transform infrared spectroscopy (FTIR), scanning electron microscopy (SEM), transmission electron microscopy (TEM), and energy-dispersive X-ray spectroscopy (EDX) to confirm its structural, morphological and compositional features. The objectives are to increase the adsorption efficiency through surface functionalization; to investigate the influence of key operational parameters such as pH, contact time, adsorbent dosage, and concentration; and to evaluate the kinetics, isotherms, stability and reusability of the synthesized adsorbent. Overall, this work seeks to provide a cost-effective, eco-friendly and sustainable strategy for antibiotic remediation and water purification applications.

2. Experimental

2.1 Chemical reagents

Doxycycline (98% purity, CAS No: 3219-99-6) was obtained from Sigma-Aldrich. A summary of its chemical and physical properties is provided in Table 1. Formic acid (FA) and MS-grade acetonitrile (ACN) were purchased from AppliChem GmbH, Germany. Potassium permanganate ($KMnO_4$; CAS No: 772264-7) with 99.0% purity and sulfuric acid (H_2SO_4; 95–97%, CAS: 7664-93-9) were obtained from Scharlau, Spain. Ethanol (C_2H_5OH; 98%, CAS No. 64-17-5) and hydrochloric acid (HCl; 37%, CAS No. 7647-01-0) were obtained from AppliChem, Germany. Phosphoric acid (H_3PO_4; 85%, CAS: 7664-38-2) was obtained from JANSSEN CHEMICA, Belgium, and hydrogen peroxide (H_2O_2; 30%, CAS: 7722-84-1) was obtained from Sigma-Aldrich. Throughout the study, all the solutions were prepared with deionized (DI) water with a resistivity of 18 MΩ cm.

2.2 Instruments

For the analysis of the DOX samples, an Agilent liquid chromatographic apparatus (1290 Infinity II) coupled with a triple-stage quadrupole mass analyzer (6420LC/TQ) was used. Molecular separation was accomplished through a ZORBAX RRHD Eclipse Plus C18 analytical column (dimensions: 2.1 × 100 mm, particle diameter: 1.8 μm). The dual-component mobile medium comprised 0.1% formic acid dissolved in aqueous solution (A) and acetonitrile (B) and was transported at a steady volumetric rate of 0.45 mL min^{-1}. Isocratic gradient elution was executed utilizing equal proportions (50% each) of components A and B. Target compound detection employed positive-mode electrospray ionization (ESI+) within liquid chromatography–tandem mass spectrometric analysis (LC–MS/MS). Multiple reaction monitoring (MRM) was implemented using a parent ion ($M + H^+$) at *m*/*z* 445.2, producing fragment ions at *m*/*z* 428.4 and 154.0. The corresponding collision

Table 1 Physicochemical properties of DOX[44]

Property	Values
Molecular formula	$C_{22}H_{24}N_2O_8$
Molecular weight	444.4 g mol^{-1}
Specific gravity	1.6
Melting temperature	201 °C
Boiling temperature	762 °C
Water solubility	630 mg L^{-1}
Dissociation constant (pKa)	pKa1 = 3.02, pKa2 = 7.97, pKa3 = 9.15
Polar surface area	181.62 $Å^2$
Molecular structure	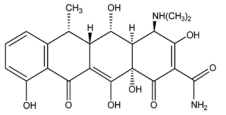

energies (CEs) were set at 20 eV and 35 eV, with a dwell voltage of 110 V applied for both transitions. The atomic composition and topographical features of GO/Fe-SBT were examined through transmission electron microscopy (TEM, Talos F200X G2, Thermo Fisher Scientific) at an acceleration potential of 200 kV. The samples were subsequently analyzed by scanning electron microscopy (SEM, EVO 18, Carl Zeiss AG, Germany) operating at 15 kV and integrated with energy-dispersive X-ray spectroscopy (EDX). Infrared absorption spectra of GO and GO/Fe-SBT were captured with a SHIMADZU IRPrestige-21 spectrometer to identify chemical moieties within the samples. X-ray diffraction (XRD) data were recorded *via* an X-ray diffractometer (SmartLab SE, Rigaku, Japan) equipped with a Cu Kα radiation source ($\lambda = 1.541$ Å).

2.3 Collection of graphite powder and GO synthesis

The used dry-cell batteries were sourced from local recycling centres and electronics repair shops. The recovery process for extracting graphite from these batteries has been thoroughly described in our previous reports.[39,45] GO was prepared from reclaimed graphite powder following a modified Hummers procedure.[39,46,47] In brief, 1 g of graphite powder was dispersed into a 9 : 1 solution of concentrated H_2SO_4 (120 mL) and H_3PO_4 (14 mL) under continuous agitation. Afterwards, 6 g of $KMnO_4$ was carefully introduced while maintaining magnetic stirring. The reaction mixture was then kept at 50 °C for 6 h until a dark green color appeared. The mixture was subsequently allowed to cool to ambient temperature and transferred into an ice bath, where 400 mL of water was slowly incorporated, followed by the dropwise addition of 3 mL of 30% H_2O_2 under stirring to neutralize the unreacted $KMnO_4$. Since the process was exothermic, the temperature was strictly controlled at approximately 0 °C *via* an ice bath. The obtained dispersion was centrifuged at 4000 rpm, and the solid residue was successively rinsed with 30% HCl solution to remove residual metal ions, further with water to reduce chloride traces, and finally with ethanol to eliminate remaining contaminants. Finally, the obtained GO was subjected to vacuum drying at 45 °C for 48 h.

2.4 Fabrication of GO/Fe-SBT

Initially, 80 mg of graphene oxide was suspended in 50 mL of DI water and subjected to ultrasonication for 35 minutes. Moreover, 0.02 mol (7.998 g) of $Fe_2(SO_4)_3 \cdot 7H_2O$ and 0.01 mol (2.781 g) of $FeSO_4 \cdot 7H_2O$ were dissolved in 100 mL of DI water and ultrasonicated for 35 minutes under ambient conditions. In parallel, 80 mg of sorbitol was solubilized in 50 mL of DI water. The graphene oxide dispersion, aqueous sorbitol, and Fe^{2+}/Fe^{3+} ion solution were subsequently mixed in a round-bottom flask and subjected to thermal treatment in an oil bath maintained at 85 °C. A 2.0 M sodium hydroxide solution was introduced dropwise to raise the pH to approximately 11, and the reaction mixture was maintained at 85 °C with continuous agitation for 2 hours. After cooling to ambient temperature, the precipitate was repeatedly rinsed with DI water until a neutral pH was achieved, followed by washing with ethanol. Finally, the product was dried in a vacuum oven at 60 °C for 18 hours to obtain the GO/Fe-SBT composite. A schematic representation of the preparation process is shown in Scheme 1.

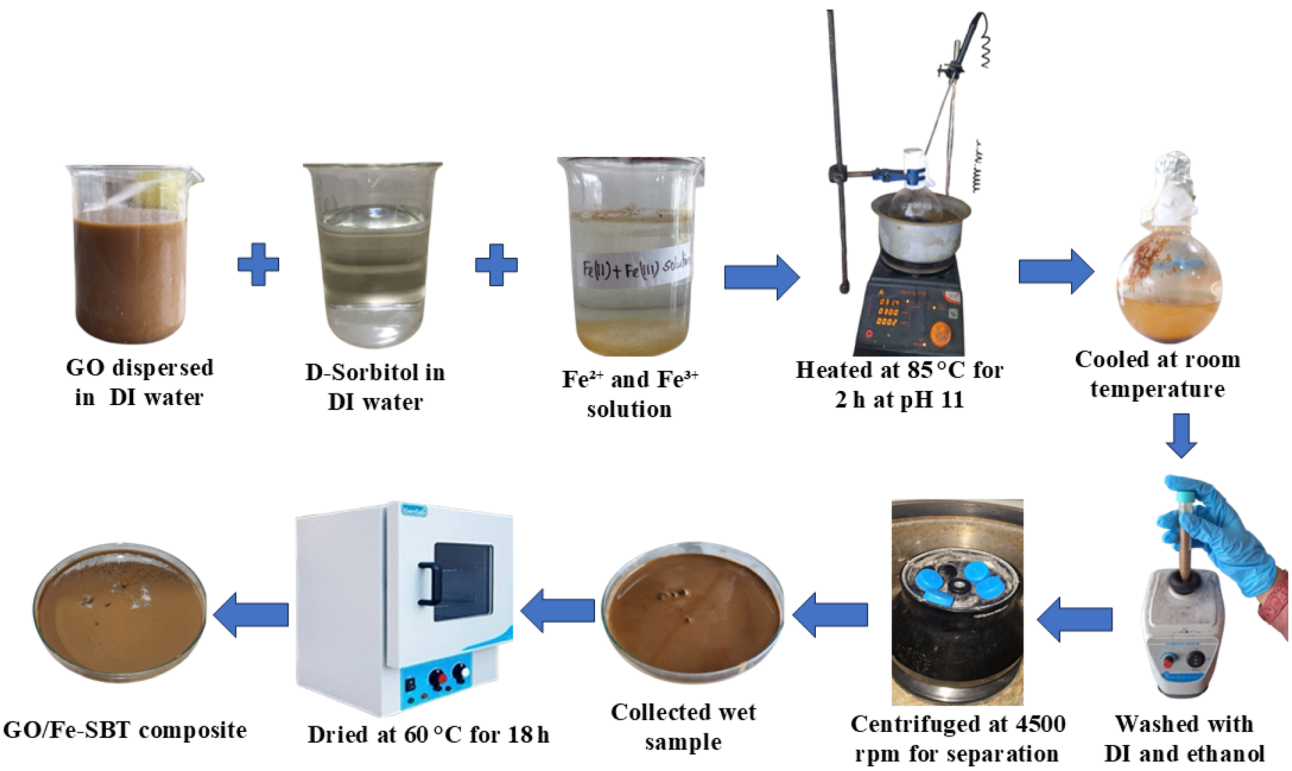

Scheme 1 Illustration of the fabrication process for the GO/Fe-SBT composite.

2.5 Adsorption studies

To conduct adsorption isotherm analysis, an accurately measured and preweighed amount of the GO/Fe-SBT composite was dispersed in 20 mL of DOX solution in a 250 mL conical flask at a controlled room temperature (298 K). To prevent any potential degradation or secondary adsorption due to light exposure, all sample flasks were wrapped in aluminum foil during the experiments. The flasks were subsequently agitated at 250 rpm in a temperature-controlled shaker to provide adequate interaction duration for the adsorption process to reach a steady state. Afterward, the suspensions were centrifuged at 4500 rpm for 5 min, allowing the solid material to be isolated from the liquid phase. The obtained liquid phases were passed through 0.22 μm CHROMAFIL® Xtra syringe filters to remove any residual solid particles. For each concentration, duplicate samples were prepared *via* the same procedure, except that the adsorbent was omitted from the control samples. The concentrations of DOX before and after the adsorption process were analyzed *via* LC–MS/MS. The adsorption behavior of DOX at various pH values was assessed over a wide pH range (3–10) following the same procedure as previously described. The pH of each solution was adjusted by the addition of 0.1 M NaOH or HCl. The influence of adsorbent dosage (1, 1.5, 2, 3, 5, 7, and 10 mg) at 298 K was analyzed to identify the optimal amount of adsorbent. In the kinetic studies, the contact time was varied between 1 and 30 min, whereas in the thermodynamic analysis, the initial concentration of DOX ranged from 0.2 to 5 ppm and was assessed at three different temperatures (25, 30, and 40 °C). The percentage of DOX removed, the quantity of DOX adsorbed at any specific time interval (q_t), and the maximum adsorption capacity at equilibrium (q_e) were determined through the application of eqn (1)–(3) as follows:[40,47]

$$\text{Removal percentage} = \frac{(C_0 - C_t)}{C_0} \times 100\% \quad (1)$$

$$q_t = \frac{(C_0 - C_t)}{M} \times V \quad (2)$$

$$q_e = \frac{(C_0 - C_e)}{M} \times V \quad (3)$$

Here C_0, C_t, and C_e denote the starting concentration, concentration at time t, and final equilibrium concentration of the DOX solution, respectively, all expressed in mg L^{-1}. The parameter V refers to the solution volume measured in liters (L), whereas M indicates the adsorbent mass expressed in grams (g).

2.6 Determination of point of zero charge (pH_{pzc})

The pH_{pzc} of the GO/Fe-SBT was evaluated by employing the solid addition method.[48] In this method, a series of 50 mL solutions of 0.01 M KCl were prepared, and their initial pH values (pH_i) were adjusted between 2.0 and 12.0 using 0.1 M HCl or 0.1 M NaOH. A fixed amount of the synthesized GO/Fe-SBT (5 mg) was then introduced into each flask, and the suspensions were agitated until equilibrium was achieved. The equilibrium pH (pH_e) of the solutions was then recorded, and the difference between the initial and equilibrium values was calculated as $\Delta pH = pH_i - pH_e$.

3. Results and discussion

3.1 Characterization of GO/Fe-SBT

3.1.1 FTIR spectral analysis. The FTIR spectra presented in Fig. 1(a) offer valuable information about the structural characteristics and molecular composition of GO and the GO/Fe-SBT composite. The spectrum of GO exhibited characteristic peaks at 3441 cm^{-1} corresponding to O–H stretching, whereas the C=O stretching peak at 1741 cm^{-1} confirmed the presence of carboxyl groups.[49] The strong band at 1633 cm^{-1} is attributed to aromatic C=C stretching, and the peak at 1058 cm^{-1} is assigned to C–O–C epoxy stretching.[50] Additionally, several pronounced bands in the 1000–1450 cm^{-1} region corresponding to C–O stretching and bending vibrations of epoxy and hydroxyl groups further confirmed the successful oxidation of GO.[50] After composite formation, significant spectral changes are observed in GO/Fe-SBT. The O–H stretching peak shifts from

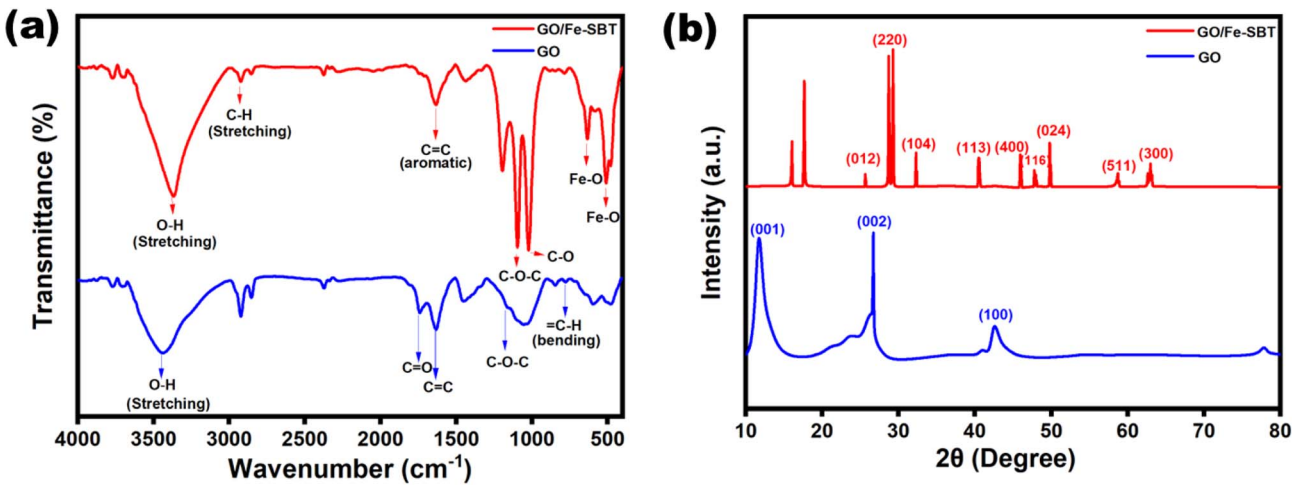

Fig. 1 (a) FTIR spectra of GO and the GO/Fe-SBT nanocomposite; (b) XRD patterns of GO and the GO/Fe-SBT nanocomposite.

3441 to 3367 cm^{-1}, indicating hydrogen bonding interactions, whereas the carbonyl peak shifts from 1741 to 1712 cm^{-1}, suggesting coordination between functional groups.[47] New Fe–O vibration bands appearing at 632, 509, and 480 cm^{-1} confirm the integration of iron oxide nanoparticles into the GO framework.[51] The enhanced C–H stretching peaks at 2857, 2926, and 2962 cm^{-1}, along with additional C–O vibrations at 1022, 1095, and 1195 cm^{-1}, provide clear evidence of the integration of sorbitol into the composite structure.[52] The persistence of the 1633 cm^{-1} band indicates that the graphene framework remains intact. Overall, these spectral features confirm the successful incorporation of Fe nanoparticles and sorbitol onto the GO surface.

3.1.2 XRD analysis. Fig. 1(b) shows the XRD patterns, which reveal the crystallographic properties of the synthesized GO and the GO/Fe-SBT composite. In the XRD profile of pristine GO, sharp peaks appeared at 2θ = 11.88°, 26.5°, and 42.45°, which are indexed to the (001), (002), and (100) planes of graphene oxide, respectively.[50,53] The prominent peak at 11.88° confirms the successful oxidation of graphite with an interlayer spacing of approximately 7.4 Å.[54] The expansion of the interlayer distance from 3.4 Å in graphite is attributed to the intercalation of oxygenated functional groups within the interlayer region.[55]

As observed in the XRD pattern, the GO/Fe-SBT composite presents a complex set of diffraction peaks, which indicate the coexistence of sorbitol-functionalized graphene-derived carbon structures and crystalline iron oxide nanophases. Distinct diffraction peaks appear at 2θ = 29.285°, 45.948°, 58.716°, and 62.638°, indexed to the (220), (400), (511), and (440) planes, respectively, indicating well-crystallized magnetite (Fe_3O_4) nanoparticles (JCPDS card no. 19–0629).[56] The XRD pattern also reveals sharp reflections at 2θ = 25.629°, 32.285°, 40.855°, 47.789°, 49.792° and 63.001°, which correspond to the (012), (104), (113), (116), (024) and (300) planes, respectively, and are consistent with the hematite (α-Fe_2O_3) phase of iron oxide (JCPDS card no. 39-1346).[57] These peak assignments indicate that mixed-phase iron-oxide nanoparticles formed within the GO matrix. The low-angle peaks at 2θ = 16.043° and 17.659° can be reasonably attributed to coordination interactions between Fe ions and sorbitol molecules. These diffraction features are characteristic of crystalline iron–polyol complexes, where the multiple hydroxyl groups of sorbitol chelate iron, giving rise to broad signals in the ~15–20° region.[58] This evidence strongly indicates the formation of Fe-sorbitol interactions within the composite matrix.

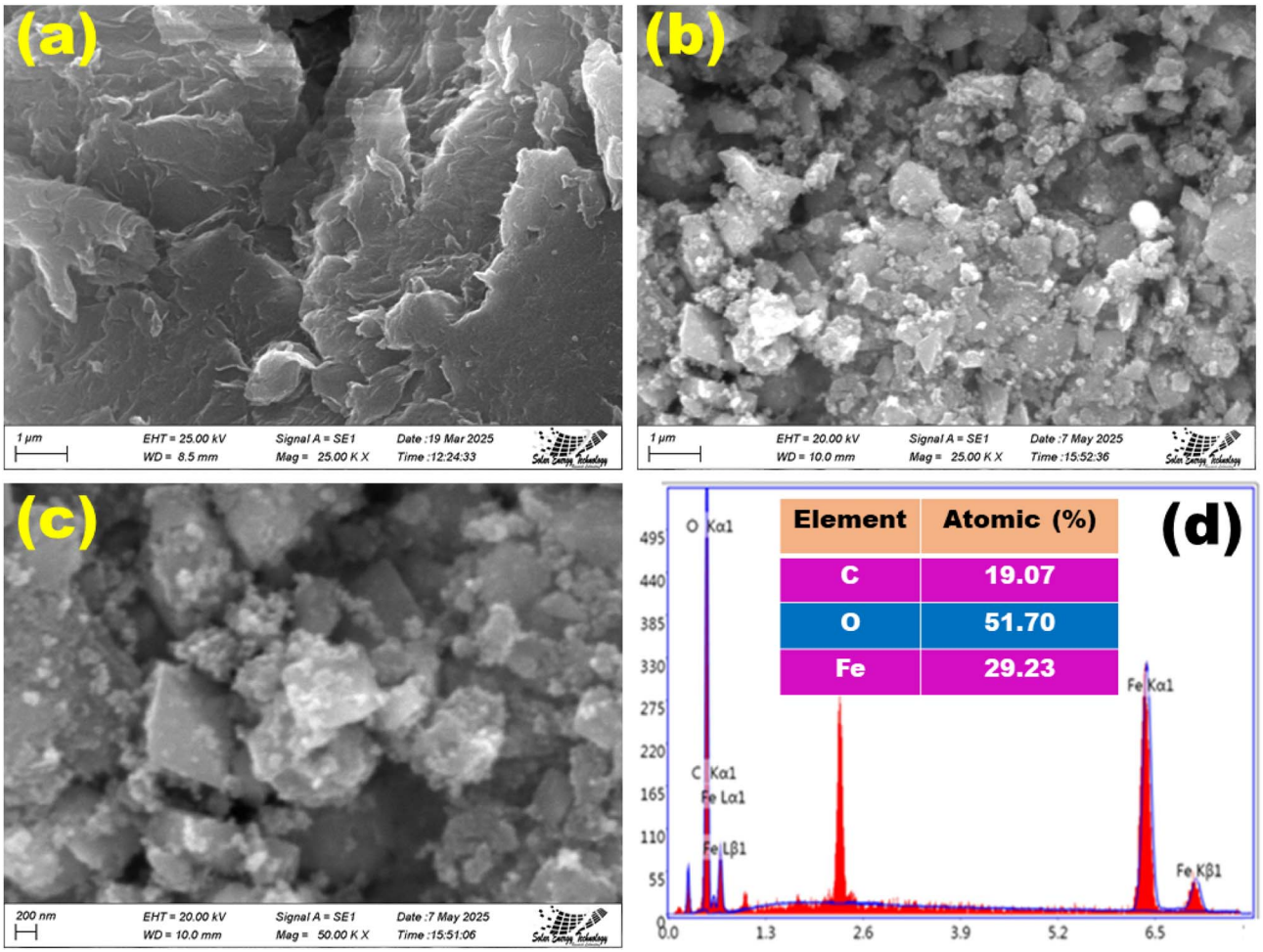

Fig. 2 (a) SEM images of GO; and (b and c) the GO/Fe-SBT nanocomposite; (d) EDX spectra of the GO/Fe-SBT nanocomposite.

3.1.3 SEM and EDX analysis. The SEM images presented in Fig. 2(a–c) reveal the morphology of GO and the GO/Fe-SBT nanocomposite. The image in Fig. 2(a) shows that the synthesized graphene oxide has a wrinkled, sheet-like structure with distinct folds and overlapping thin flakes. The sheets are randomly stacked and agglomerated, forming a layered network. The surface appears rough and ridged, presumably resulting from oxygen-bearing functional moieties introduced during oxidation that alter the fundamental structural plane.[30] The SEM image of the GO/Fe-SBT composite (Fig. 2(b and c)) reveals densely packed, irregularly shaped particles aggregated into a compact network. The particles display a rough surface texture, which may result from the incorporation of iron oxide nanoparticles into the wrinkled graphene oxide sheets, which are further stabilized by sorbitol functionalization. The effective anchoring of iron oxide onto the graphene oxide surface enhances the available surface area and provides numerous reactive sites. The corresponding EDX spectrum in Fig. 2(d) confirms the elemental composition of the GO/Fe-SBT composite. The high oxygen content can be attributed to the oxygen-bearing functional moieties of graphene oxide and sorbitol, as well as the presence of iron oxide. The substantial Fe content confirms the successful incorporation of iron oxide nanoparticles, whereas the carbon signal arises from the graphene oxide backbone and the sorbitol modifier. These results collectively verify the successful synthesis of the GO/Fe-SBT composite with a uniform distribution of its constituent elements.

3.1.4 TEM analysis. The TEM image of the GO/Fe-SBT nanocomposite (Fig. 3(a)) reveal that iron oxide nanoparticles are uniformly distributed and anchored onto the wrinkled, sheet-like structure of graphene oxide, indicating that sorbitol functionalization effectively prevents excessive agglomeration and promotes homogeneous dispersion. The nanoparticles exhibit a nearly spherical morphology with an average size of 5-8 nm, as shown in the particle size distribution histogram (Fig. 3(b)). The HRTEM image (Fig. 3(c)) further confirms the crystalline nature of the nanoparticles, with a distinct lattice

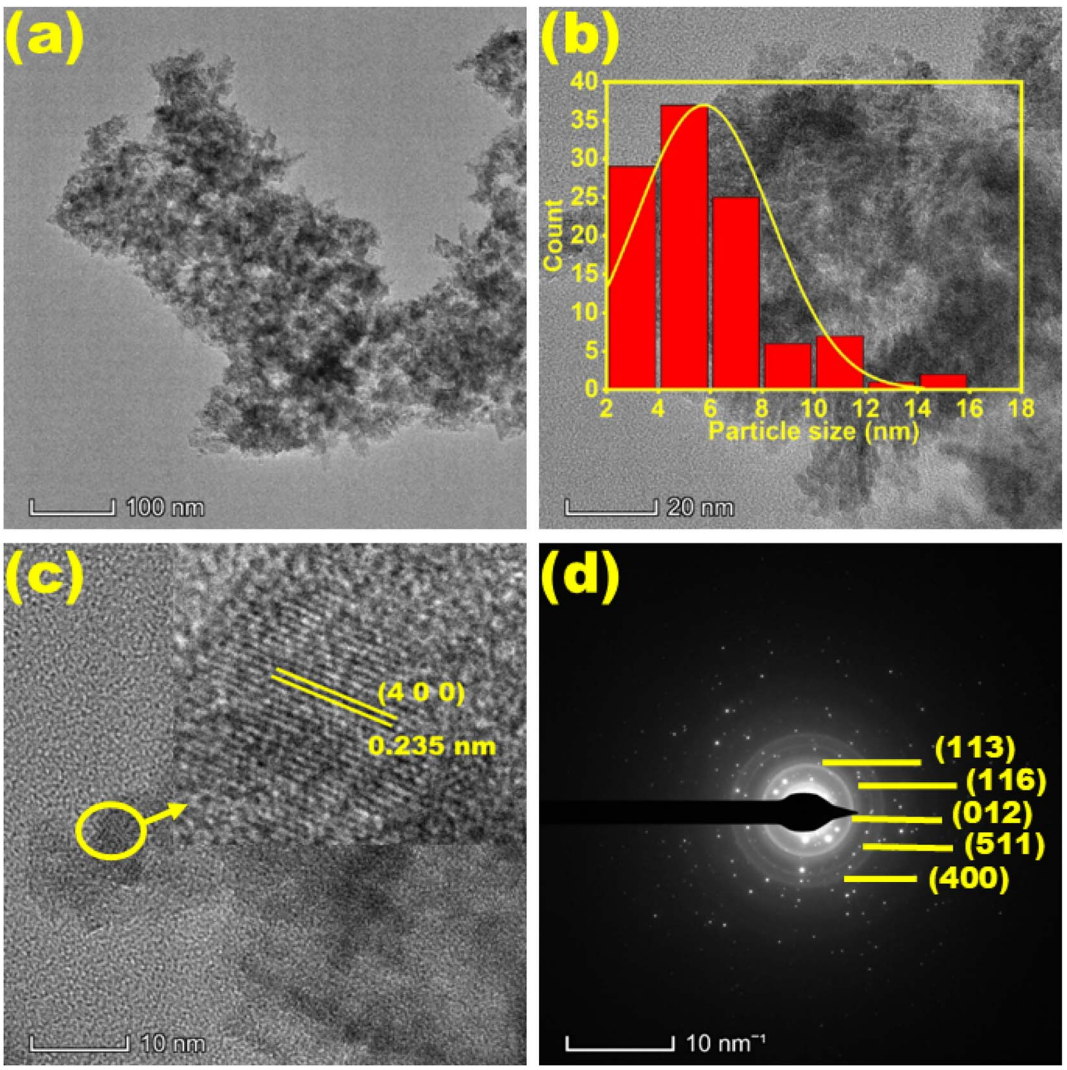

Fig. 3 (a) TEM micrograph of the GO/Fe-SBT nanocomposite; (b) particle size distribution histogram derived from TEM analysis; (c) high-resolution images showing the lattice fringes of the Fe_3O_4 nanoparticles and (d) SAED pattern corresponding to the GO/Fe-SBT nanocomposite.

fringe spacing of 0.235 nm corresponding to the (400) plane of magnetite (Fe_3O_4), which is consistent with the XRD results. The selected area electron diffraction (SAED) pattern (Fig. 3(d)) displays sharp concentric diffraction rings indexed to the (012), (113), (116), (440), and (511) planes of iron oxide, confirming the polycrystalline nature of the nanoparticles. These diffraction patterns support the findings from the XRD study, confirming that both crystalline magnetite and hematite phases are present together within the composite material.

3.2 Adsorption of DOX by the GO/Fe-SBT nanocomposite

3.2.1 Effect of the adsorbent dose. A key objective of the adsorbent dosage experiments is to optimize the amount of material used, ensuring that no excess adsorbent is wasted once equilibrium is achieved. DOX adsorption behavior in response to adsorbent dosage was evaluated by altering the GO/Fe-SBT amount between 1 and 10 mg while keeping all other experimental conditions constant. The findings presented in Fig. 4(a) reveal that the adsorption curve follows two distinct stages, beginning with a rapid increase and progressing to steady linear growth. During the initial rapid increase phase, the removal efficiency of DOX improved significantly from 84.73% to 96.82% as the adsorbent dose increased from 1 mg to 2 mg. The increase in adsorbent quantity improved the accessibility of the reactive sites, thus promoting the attachment of DOX molecules to the adsorption surface more efficiently.[53] However, when the dose surpassed 3 mg, no additional improvement in removal efficiency was observed, implying equilibrium conditions. The dose that ensured high adsorption without excessive adsorbent consumption was 0.1 g L^{-1}. Therefore, 0.1 g L^{-1} of GO/Fe-SBT was employed in the subsequent experimental trials.

3.2.2 Effect of contact time. The contact duration is a major determinant of adsorption and reflects the underlying mechanism. To examine its impact on DOX removal, a series of trials with contact times between 1 and 30 min were conducted under constant conditions (25 °C, 0.1 g L^{-1} adsorbent, pH 5, C_0 =

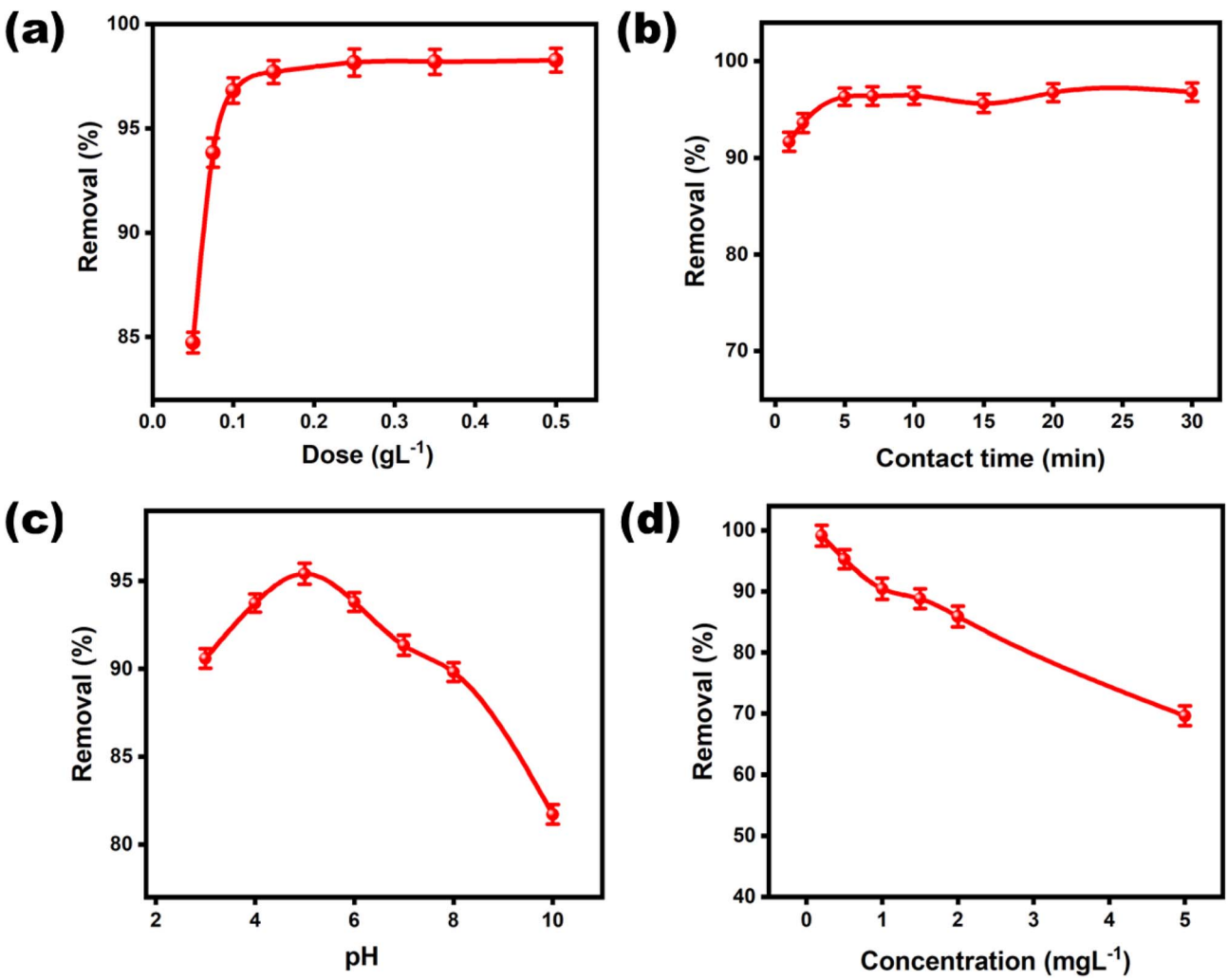

Fig. 4 (a) Effect of GO/Fe-SBT composite dosage on DOX removal from aqueous solution (t = 5 min, pH = 5, C_o = 200 ppb, T = 25 °C, shaking speed = 250 rpm), (b) effect of time on removal efficiency (dose = 0.1 g L^{-1}, pH = 5, C_o = 200 ppb, T = 25 °C, shaking speed = 250 rpm), (c) effect of pH on removal efficiency (dose = 0.1 g L^{-1}, t = 5 min, C_o = 200 ppb, T = 25 °C, shaking speed = 250 rpm), (d) effect of concentration on removal efficiency (dosage = 0.1 gL^{-1}, t = 5 min, pH = 5, T = 25 °C, shaking speed = 250 rpm).

0.2 ppm, 250 rpm). As illustrated in Fig. 4(b), the removal efficiency increased rapidly at the beginning, reaching approximately 91.67% within the first minute. This efficiency increased sharply to over 96.35% within the first five minutes, after which it gradually stabilized and remained nearly constant up to 30 minutes. The rapid adsorption observed in the initial stages results from the plentiful accessible active sites present at the GO/Fe-SBT interface, which promotes quick molecular interactions between the adsorbent and DOX molecules. With increasing time, the active sites progressively become occupied, leading to saturation and a subsequent reduction in removal efficiency.[59] Notably, adsorption equilibrium was attained rapidly, within 5 minutes; therefore, 5 minutes was determined to be the optimum contact time for adsorption. This behavior indicates that, beyond a certain duration, adsorption is highly efficient and essentially time independent, which is advantageous for practical applications.

3.2.3 Effect of pH. The solution pH significantly affects antibiotic adsorption by altering the adsorbent surface charge and the ionization state of the adsorbate. In this study, DOX adsorption onto a GO/Fe-SBT nanocomposite was investigated over a pH range of 3-10. The results are presented in Fig. 4(c). As shown, the removal efficiency increased from 90.60% at pH 3 to a maximum of 95.42% at pH 5, indicating that mildly acidic conditions are most favorable for DOX adsorption onto the GO/Fe-SBT composite. The point of zero charge (pH_{pzc}) of the GO/Fe-SBT nanocomposite was determined to be 5.3, implying that the composite surface carries a net positive charge below this value and a negative charge above it. At pH 3, DOX exists mainly in cationic form (DOX^{3+}/DOX^{+}), while the protonated composite surface is also positively charged, leading to strong electrostatic repulsion and lower adsorption.[60] As the pH increases toward 5.0, DOX gradually converts into its zwitterionic form, while the surface charge of the composite becomes less positive. This facilitates favorable interactions between the partially negative groups of DOX and the composite surface, which are further reinforced by hydrogen bonding and π–π stacking, resulting in the highest adsorption at pH 5. Beyond the pH_{pzc}, the adsorbent surface acquires a negative charge, while DOX progressively converts to anionic species (DOX^{-}, DOX^{2-}). This charge incompatibility enhances electrostatic repulsion between the adsorbent and adsorbate, resulting in

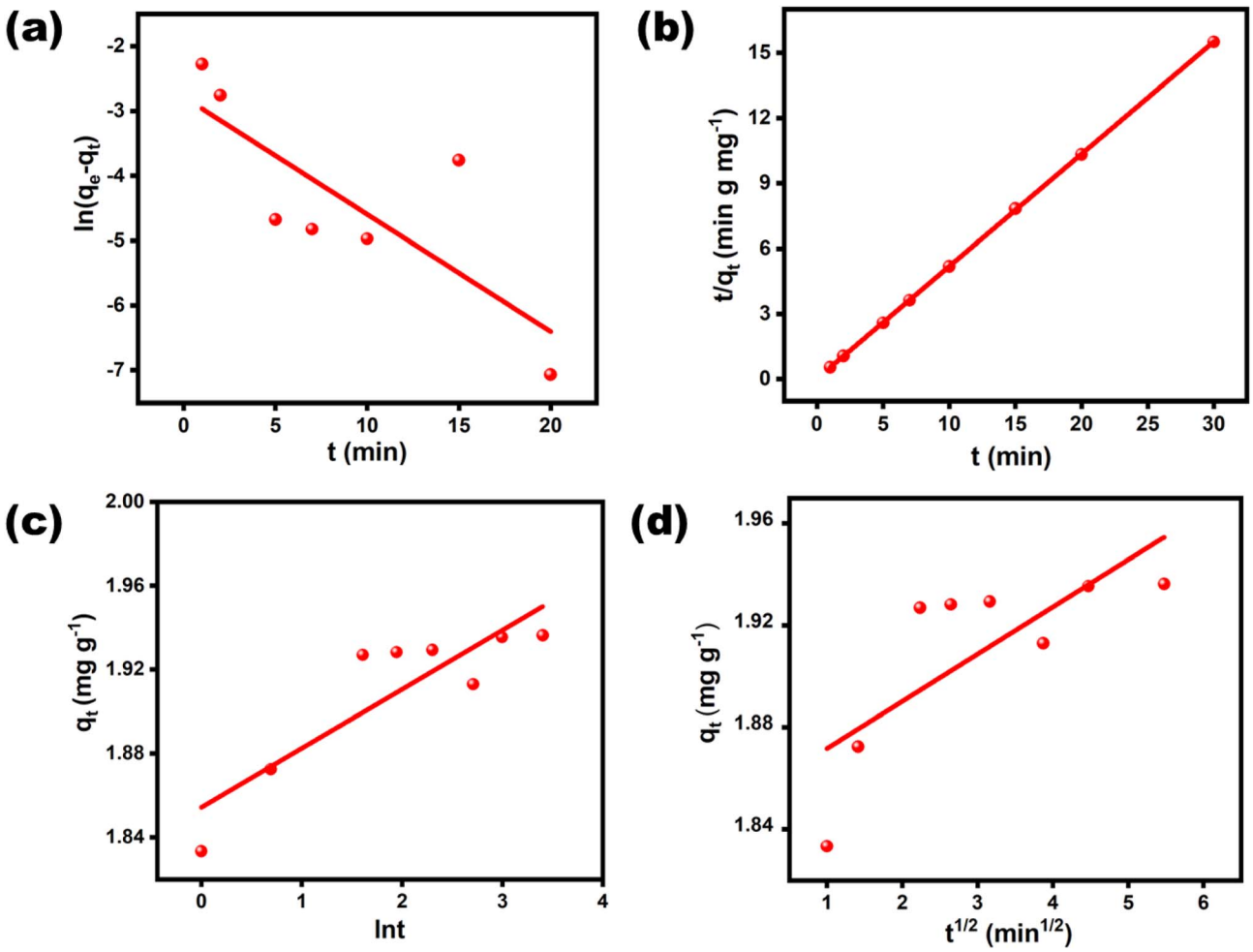

Fig. 5 (a) Linear pseudo-first-order kinetics model (b) linear pseudo-second-order kinetics model (c) Elovich kinetic model (d) Weber-Morris intraparticle diffusion model (GO/Fe-SBT = 0.1 g L^{-1}, t = (1–30) min, pH = 5, C_0 = 200 ppb, T = 25 °C, shaking speed = 250 rpm).

a gradual decline in adsorption efficiency with increasing pH. Consequently, considering the above analysis and the highest recorded removal efficiency, pH 5 was determined to be the most favorable condition for the adsorption process.

3.2.4 Effect of concentration. The initial adsorbate concentration strongly influences both removal efficiency and adsorption capacity. The availability of adsorbate molecules in solution affects the accessibility of binding sites, the activity of functional groups and the extent of various interaction mechanisms. The effect of initial DOX concentration on the adsorption performance of the GO/Fe-SBT nanocomposite was evaluated over a concentration range of 0.2 to 5 mg L^{-1}. As shown in Fig. 4(d), the removal efficiency reached a maximum of 99.15% at an adsorbate concentration of 0.2 mg L^{-1}, but declined to 69.65% when the concentration increased to 5 mg L^{-1}. The observed trend implies that lower initial concentrations provide the adsorbent with enough active sites, thereby enhancing the adsorption efficiency.[47] However, as the concentration of DOX increases, the adsorption sites become saturated, and the mass transfer resistance increases, which reduces the overall efficiency.[33] Thus, the GO/Fe-SBT nanocomposite achieves optimal adsorption at 0.2 mg L^{-1}.

Table 2 Kinetic model-derived parameters

Kinetics model (linear)	Parameters	Value
Pseudo-first-order	q_e (mg g^{-1})	0.06212
	k_1(min^{-1})	0.18107
	R^2	0.62053
Pseudo-second-order	q_e (mg g^{-1})	1.93850
	k_2 (g mg^{-1} min^{-1})	8.17053
	R^2	0.99997
Elovich	α (mg g^{-1} min^{-1})	1.063×10^{27}
	β (g mg^{-1})	35.48616
	R^2	0.77446
Weber-Morris intraparticle diffusion	k_i (mg g^{-1} $min^{-1/2}$)	0.01852
	C_i (mg g^{-1})	1.85322
	R^2	0.58054

3.2.5 Kinetic studies. For a detailed elucidation of the adsorption mechanism, the obtained experimental data were analyzed within the framework of different kinetic models, including the Lagergren pseudo-first-order, Ho's pseudo-second-order, Elovich, and Weber-Morris intraparticle

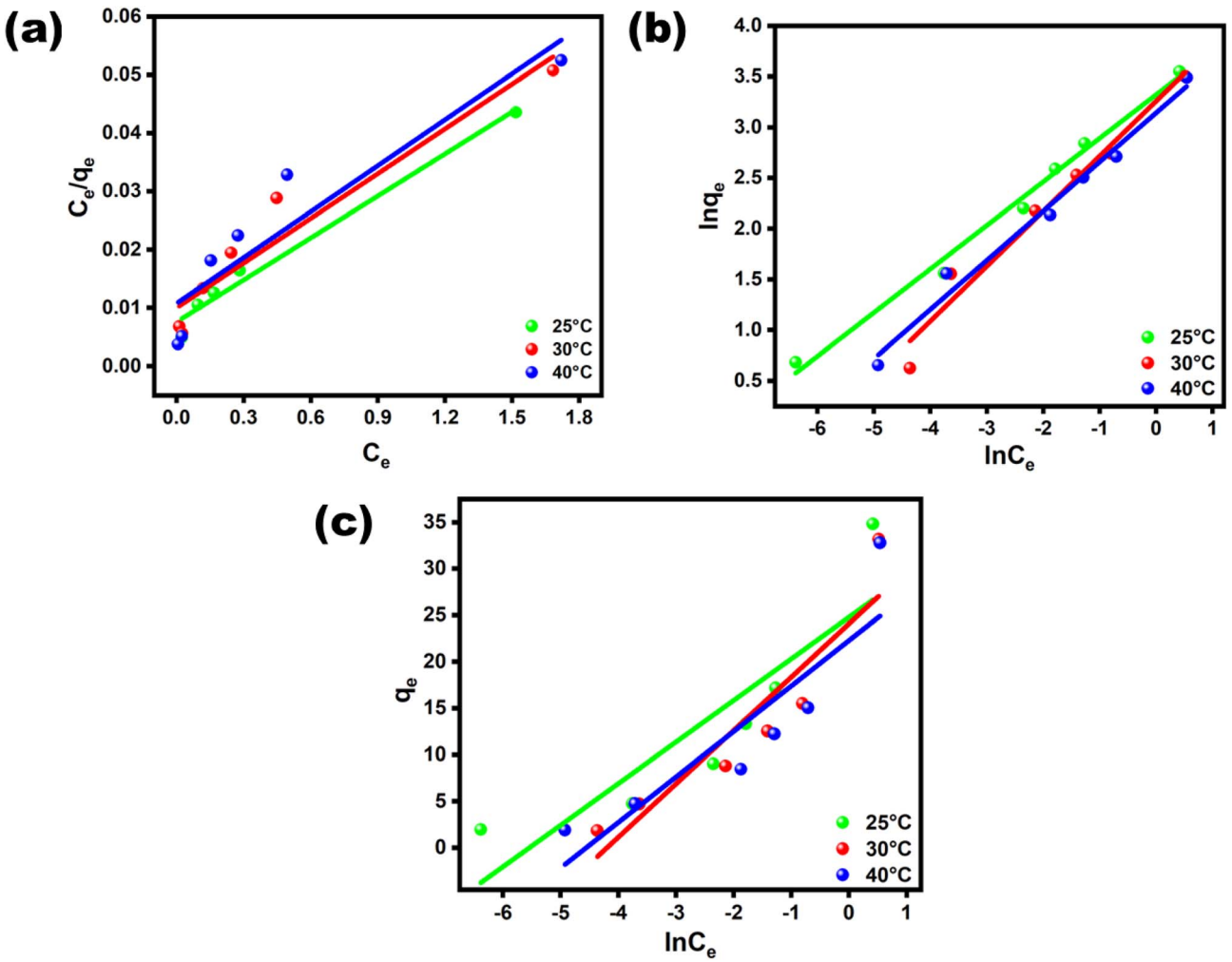

Fig. 6 Isotherm studies of GO/Fe-SBT by the (a) Langmuir isotherm, (b) Freundlich isotherm, and (c) Temkin isotherm.

diffusion models. These kinetic models are illustrated graphically in Fig. 5, and their corresponding linearized equations are provided in eqn (4)–(7):[53]

$$\ln(q_e - q_t) = \ln q_e - k_1 t \quad (4)$$

$$\frac{t}{q_t} = \frac{1}{k_2 {q_e}^2} + \frac{t}{q_e} \quad (5)$$

$$q_t = \frac{1}{\beta}\ln(\alpha\beta) + \frac{1}{\beta}\ln\, t \quad (6)$$

$$q_{t=k_i t^{0.5}} + C_i \quad (7)$$

Here, q_e denotes the amount of adsorbate adsorbed at equilibrium (mg g^{-1}), whereas q_t represents the adsorption capacity at a given time t (mg g^{-1}). k_1 is the rate constant of the pseudo-first-order kinetic model, expressed in min^{-1}, and k_2 refers to the rate constant of the pseudo-second-order model, with units of g mg^{-1} min^{-1}. The constant α represents the initial adsorption rate (mg g^{-1} min^{-1}), whereas β is associated with surface coverage and the activation energy of the chemisorption process (g mg^{-1}). k_i denotes the rate constant for the intraparticle diffusion model, expressed in mg g^{-1} $min^{-1/2}$. The parameter C_i is a constant that reflects the boundary layer effect and is proportional to its thickness, expressed in mg g^{-1}.

The kinetic parameters derived from various models are compiled in Table 2. Among these, the pseudo-second-order kinetic model, depicted in Fig. 5(b), demonstrates the best fit to the experimental data, as evidenced by a superior correlation coefficient (R^2) of 0.999. This indicates strong agreement between the observed results and the theoretical linear form of the model. The excellent fit to second-order kinetics implies that the adsorption process is predominantly governed by chemisorption, where chemical interactions between the adsorbate and the adsorbent surface play a key role in the rate-determining step.

3.2.6 Isotherm studies. Isothermal adsorption analysis serves as an essential tool for assessing the adsorption efficiency of an adsorbent. Additionally, it offers important information about the fundamental molecular mechanisms governing adsorbate–adsorbent interactions. The isothermal adsorption study was carried out at three different temperatures (25, 30, and 40 °C) using DOX concentrations ranging from 0.2 to 5 mg L^{-1}. Equilibrium adsorption results were evaluated using the Langmuir, Freundlich, and Temkin isotherm models. The corresponding graphical plots are shown in Fig. 6, and the linear forms of these isotherms (eqn (8)–(10)) are outlined below:[33]

$$\text{Langmuir equation}: \frac{C_e}{q_e} = \frac{1}{K_L q_m} + \frac{C_e}{q_m} \quad (8)$$

$$\text{Freundlich equation}: \ln\, q_e = \ln\, K_F + \frac{1}{n}\ln\, C_e \quad (9)$$

$$\text{Temkin equation}: q_e = \frac{RT}{b}\ln\, K_T + \frac{RT}{b}\ln\, C_e \quad (10)$$

Here, q_e refers to the amount of antibiotic adsorbed at equilibrium per unit mass of adsorbent (mg g^{-1}), whereas C_e indicates the concentration of the antibiotic remaining in the solution at equilibrium (mg L^{-1}). The constant R represents for the molar gas constant, which is 8.314 J mol^{-1} K^{-1} and q_m represents the theoretical maximum amount of DOX that can be adsorbed per unit mass of the GO/Fe-SBT composite. In the Langmuir isotherm model, the constant K_L (L mg^{-1}) represents the adsorption energy and the affinity between the adsorbate and adsorbent. In contrast, for the Freundlich isotherm, K_F ($mg^{1-1/n}$ $L^{-1/n}$ g^{-1}) indicates the adsorption capacity, whereas the exponent $1/n$ reflects the degree of surface heterogeneity. In the Temkin isotherm model, K_T (L g^{-1}) denotes the equilibrium binding constant, whereas b (J mol^{-1}) corresponds to the Temkin constant associated with the heat of adsorption.

The analysis of isotherm parameters obtained from the linearized expressions of the Langmuir, Freundlich, and Temkin models, as presented in Table 3, indicates that the Freundlich model most accurately describes the DOX adsorption behaviour on the GO/Fe-SBT composite. This finding is validated by the greater R^2 value (0.99) of the Freundlich model than those of the Langmuir (0.98) and Temkin (0.78) models. These findings suggest that the adsorption phenomenon involves multilayer molecular accumulation on the adsorbent material. The adsorbent surface has a heterogeneous distribution of active binding sites, enabling adsorption *via* ion exchange mechanisms involving functional groups such as $-COO^-$ and –OH. Furthermore, the Freundlich parameter n, indicating adsorption favorability, exceeded unity across all the tested temperatures, with values of 1.84, 2.06, and 2.32 at 25 °C, 30 °C, and 40 °C, respectively. This finding demonstrated that DOX adsorption onto the GO/Fe-SBT nanocomposite represents a favorable and effective process. Linear Langmuir analysis yielded maximum adsorption capacities (q_m) of 41.61, 39.06, and 38.05 mg g^{-1} at 25 °C, 30 °C, and 40 °C, respectively.

3.2.7 Stability and reusability studies. Adsorbent stability and reusability are vital characteristics that are fundamental to achieving economic viability and environmental sustainability. Therefore, the stability and reusability of the adsorbent were evaluated over seven successive adsorption–desorption cycles. After DOX adsorption was complete, the GO/Fe-SBT material was efficiently restored by methanol washing treatment. In this process, the adsorbent was separated by centrifugation, washed

Table 3 Comparative study of isotherm model parameters (Langmuir, Freundlich, and Temkin) for DOX adsorption by GO/Fe-SBT

Isotherm model	Parameters	25 °C	30 °C	40 °C
Langmuir	q_m (mg g^{-1})	41.61	39.06	38.05
	K_L (L mg^{-1})	3.17	2.56	2.44
	R^2	0.9822	0.9248	0.8706
Freundlich	n	2.32	1.84	2.06
	K_F ($mg^{1-1/n}$ $L^{-1/n}$ g^{-1})	27.72	26.01	23.17
	R^2	0.9896	0.9685	0.9831
Temkin	K_T (L g^{-1})	255.33	66.50	95.31
	b (J mol^{-1})	554.26	439.29	532.46
	R^2	0.7798	0.8655	0.7926

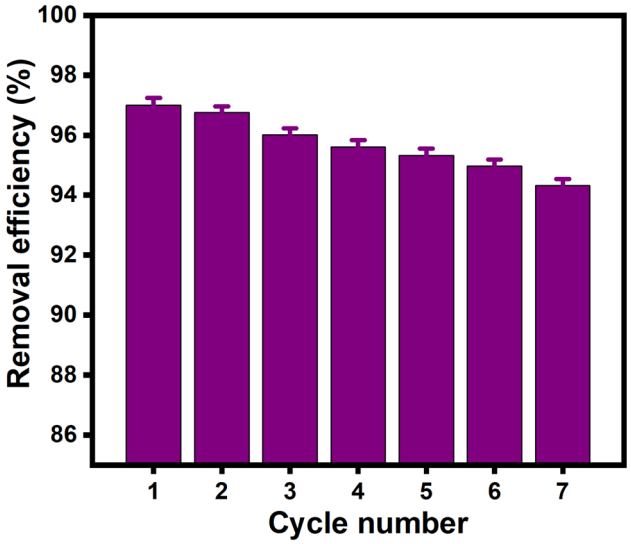

Fig. 7 Study of the stability and reusability of GO/Fe-SBT nanocomposite.

three times with methanol under ultrasonic agitation to desorb the retained DOX molecules, and then dried under vacuum oven at 60 °C for reuse in the subsequent cycle.[32] As shown in Fig. 7, the adsorbent retained more than 94% of its removal efficiency after seven consecutive regeneration cycles, exhibiting only a modest decline. This minor loss is primarily attributed to system-related losses occurring during repeated adsorption–desorption cycles, with a small contribution from partial surface fouling. Post-cycle FTIR and SEM-EDX analyses (Fig. S1 and S2) confirmed that the composite retained its overall functional groups, surface morphology and elemental composition. Only a slight decrease in FTIR band intensities was observed, indicating minor surface changes without significant structural degradation. These results collectively demonstrate that GO/Fe-SBT possesses strong structural and morphological stability, making it suitable for multiple adsorption cycles and enabling cost-effective regeneration.

3.2.8 Adsorption mechanism. The structure of DOX incorporates various ionizable functional units, notably alcohol, phenol, and amino functionalities. This enables the compound to adopt different ionic states, including anions, cations and zwitterions. It has multiple acid dissociation constants (pKa) and assumes a zwitterionic state at intermediate pH.[61] Below pH 3.02 (pKa1 = 3.02), DOX is predominantly in its protonated cationic form (DOX^+). At pH values between 3.02 and 7.97 (pKa2 = 7.97), zwitterionic species (DOX^0) are favoured. From pH 7.97 to 9.15 (pKa3 = 9.15), the monoanionic form (DOX^-) predominates, whereas at pH values above 9.15, the molecule is largely deprotonated to the dianion (DOX^{2-}) owing to proton loss from the phenolic diketone moiety and the tricarbonyl system.[62] The type of chemical interaction between DOX and the adsorbent is influenced by the charge present on the molecule. Under mildly acidic to near-neutral conditions, zwitterionic DOX molecules interact with the oxygen-rich surface of GO/Fe-SBT through electrostatic attraction and hydrogen bonding between the protonated $-NH_2$ groups of DOX and the deprotonated $-COO^-$ or –OH groups of GO and sorbitol.[44] The noticeable shift and broadening of the O–H stretching band in the FTIR spectrum

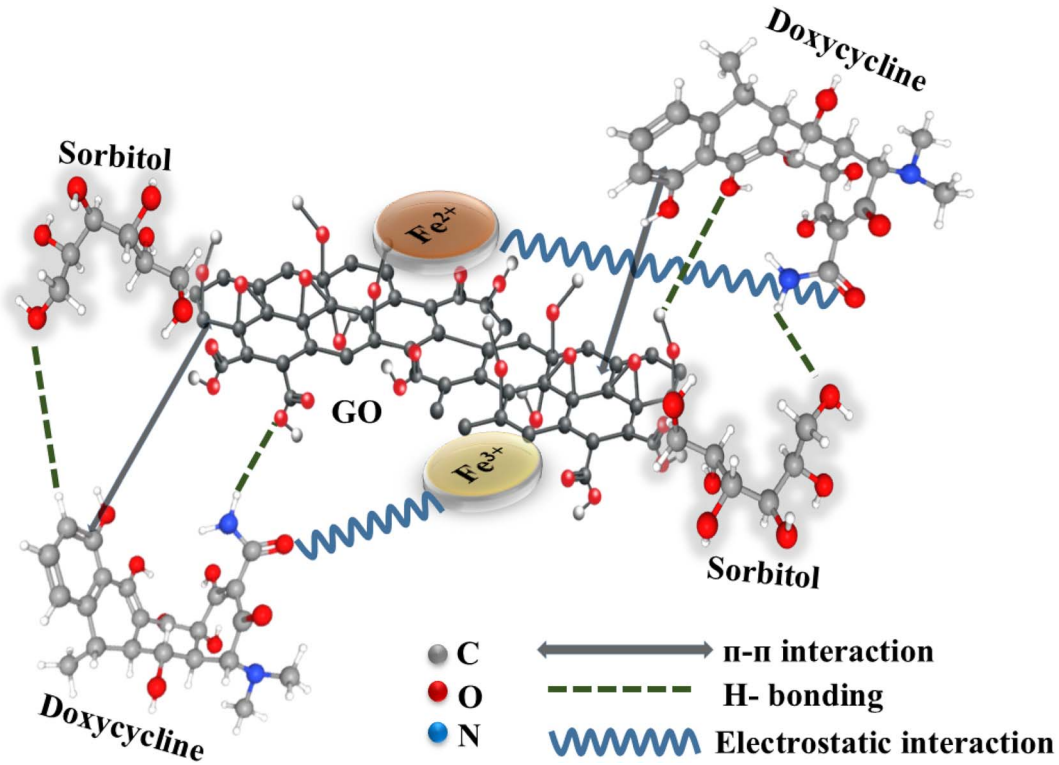

Fig. 8 Adsorption mechanism of DOX on the GO/Fe-SBT nanocomposite.

Table 4 Adsorption capacity and equilibrium time of different adsorbents for DOX removal

Adsorbent	Adsorption capacity, q_m (mg g^{-1})	Equilibrium time (min)	Temperature (°C)	pH	Ref.
Cobalt oxide	4.484	—	40	6	66
Magnetic Fe_3O_4@chitosan carbon microbeads	4.816	—	25	11	67
Graphene oxide/hydrogel composite	6.77	180	15	7	68
Electrogenerated adsorbents (EGAs)	9.130	210	—	7.65	69
GO supported Ni–Fe nano adsorbent	13.02	20	25	5	53
Rice husk ash	17.74	85.85	—	6	70
Eutectic solvent functionalized activated carbon	30.35	240	30	7.5	71
rGO/nZVI composite	31.614	60	25	7	72
Graphene nanosheet	110	200	—	6-7	73
GO/Fe-SBT nanocomposite	**41.61**	**5**	**25**	**5**	**Present study**

after adsorption (Fig. S1) support the formation of extensive hydrogen-bonding networks between DOX and surface functional groups. Additionally, the aromatic rings of DOX can engage in π–π interactions with the conjugated graphene domains of GO, which enhances the affinity of DOX for the nanocomposite surface. The persistence of Fe–O bands in the FTIR spectra (Fig. S1) indicates that the iron oxide nanoparticles remain structurally stable, continuing to serve as active coordination centers during adsorption. This enables DOX to form chelate complexes *via* Fe–O inner-sphere coordination, thereby enhancing binding strength. Similar mechanisms involving Fe-mediated coordination, π–π stacking and hydrogen bonding have been reported in related graphene and metal oxide-based adsorbents.[63–65] These combined effects contribute to the high adsorption capacity and rapid removal efficiency of the GO/Fe-SBT nanocomposite. The probable adsorption mechanism is shown Fig. 8.

3.2.9 Comparison of the GO/Fe-SBT adsorbent with other adsorbents. Table 4 compares GO/Fe-SBT nanocomposite with several reported adsorbents for DOX removal. Most of the listed adsorbents show lower adsorption capacities or require longer equilibrium times. In contrast, GO/Fe-SBT reaches a high adsorption capacity of 41.61 mg g^{-1} and attains equilibrium in only 5 minutes, highlighting its rapid and efficient adsorption performance.

4. Conclusion

In summary, an eco-friendly and highly effective GO/Fe-SBT nanocomposite was successfully synthesized and demonstrated exceptional performance in DOX removal from aqueous solutions. The adsorption process exhibited remarkable efficiency, achieving 96.82% DOX removal within 5 minutes at pH 5 using an adsorbent dosage of 0.1 g L^{-1}. Kinetic studies revealed that adsorption followed pseudo-second-order kinetics (R^2 = 0.999), indicating that chemisorption was the dominant mechanism, whereas isotherm analysis showed the best fit with the Freundlich model (R^2 = 0.989), confirming multilayer adsorption on heterogeneous surfaces. The nanocomposite exhibited a maximum adsorption capacity of 41.61 mg g^{-1}, driven by synergistic mechanisms such as hydrogen bonding, electrostatic attractions, π–π interactions and metal coordination between DOX and the oxygen-rich functional groups of the composite. The GO/Fe-SBT nanocomposite also demonstrated superior performance compared to reported adsorbents in terms of adsorption capacity and equilibrium time. Furthermore, it exhibited excellent reusability, retaining more than 94% removal efficiency after seven regeneration cycles. These results highlight the strong potential of the GO/Fe-SBT nanocomposite as an efficient and sustainable adsorbent for DOX removal from aqueous systems.

Author contributions

Afia Murshida Kusum: experimental execution, formal analysis, data curation, writing original draft. Md Humayun Kabir: conceptualization, supervision, investigation, visualization, funding acquisition, project administration. Md. Safiqul Islam: supervision, investigation, writing – review and editing. Md Sakil: data analysis, writing – review and editing. Sabina Yasmin: conceptualization, supervision, investigation, visualization, funding acquisition, project administration, writing – review and editing.

Conflicts of interest

There are no conflicts to declare.

Data availability

Data will be available on request.

Supplementary information (SI) is available. See DOI: https://doi.org/10.1039/d5ra07287e.

Acknowledgements

The authors are grateful to the Bangladesh Council of Scientific and Industrial Research (BCSIR) for financial support (R&D ref. no. 39.02.0000.011.14.180.2024/1116, date 14.01.2025) and facilities. While SEM-EDX are carried out by IERD, BCSIR; XRD and FTIR are supported by Centre for Advanced Research in

Sciences at the University of Dhaka which is praised. The authors sincerely acknowledge the Physical Chemistry Research Laboratory for their valuable experimental support.

References

1 L. Ji, F. Liu, Z. Xu, S. Zheng and D. Zhu, *Environ. Sci. Technol.*, 2010, **44**, 3116–3122.
2 I. Braschi, S. Blasioli, L. Gigli, C. E. Gessa, A. Alberti and A. Martucci, *J. Hazard. Mater.*, 2010, **178**, 218–225.
3 I. Michael, L. Rizzo, C. S. McArdell, C. M. Manaia, C. Merlin, T. Schwartz, C. Dagot and D. Fatta-Kassinos, *Water Res.*, 2013, **47**, 957–995.
4 A. K. Sarmah, M. T. Meyer and A. B. A. Boxall, *Chemosphere*, 2006, **65**, 725–759.
5 V. Homem and L. Santos, *J. Environ. Manage.*, 2011, **92**, 2304–2347.
6 N. N. A. Nuar, S. N. A. M. Jamil, T. S. Y. Choong, S. I. Mahadzir, I. D. M. Azmi, M. S. M. Basri and M. R. A. Hamid, *ACS Omega*, 2025, **10**, 10205–10219.
7 M. Z. Akbari, Y. Xu, Z. Lu and L. Peng, *Environ. Adv.*, 2021, **5**, 100111.
8 F. Ahmad, D. Zhu and J. Sun, *Environ. Sci. Eur.*, 2021, **33**, 64.
9 S. Zaidi, T. Chaabane, V. Sivasankar, A. Darchen, R. Maachi and T. A. M. Msagati, *Arab. J. Chem.*, 2019, **12**, 2798–2809.
10 W. Baran, E. Adamek, M. Jajko and A. Sobczak, *Chemosphere*, 2018, **194**, 381–389.
11 J. Rivas, Á. Encinas, F. Beltrán and N. Graham, *J. Environ. Sci. Health Part A*, 2011, **46**, 944–951.
12 S. Zaidi, T. Chaabane, V. Sivasankar, A. Darchen, R. Maachi, T. A. M. Msagati and M. Prabhakaran, *Process Saf. Environ. Prot.*, 2016, **102**, 450–461.
13 M. Hijosa-Valsero, G. Fink, M. P. Schlüsener, R. Sidrach-Cardona, J. Martín-Villacorta, T. Ternes and E. Bécares, *Chemosphere*, 2011, **83**, 713–719.
14 X. Ai, H. Fan, Y. Wang, Y. Guo, X. Liu, L. Yang, H. Liu and J. Yang, *RSC Adv.*, 2018, **8**, 36280–36285.
15 J. Gao, Y. Gao, Z. Sui, Z. Dong, S. Wang and D. Zou, *J. Alloys Compd.*, 2018, **732**, 43–51.
16 A. A. Borghi, M. F. Silva, S. Al Arni, A. Converti and M. S. A. Palma, *J. Chem.*, 2015, **2015**, 492030.
17 J. Bolobajev, M. Trapido and A. Goi, *Chemosphere*, 2016, **153**, 220–226.
18 J. O. Eniola, R. Kumar and M. A. Barakat, *Environ. Sci. Pollut. Res.*, 2019, **26**, 34775–34788.
19 J. O. Ighalo, O. J. Ajala, G. Umenweke, S. Ogunniyi, C. A. Adeyanju, C. A. Igwegbe and A. G. Adeniyi, *J. Environ. Chem. Eng.*, 2020, **8**, 104264.
20 C. A. Igwegbe, C. J. Umembamalu, E. U. Osuagwu, S. N. Oba and L. N. Emembolu, *Eur. J. Sustain. Dev. Res.*, 2020, **5**, em0145.
21 J. Bensalah, A. Idrissi, M. E. Faydy, G. Doumane, A. Staoui, R. Hsissou, A. Lebkiri, A. Habsaoui, Z. Abdelkader and E. H. Rifi, *J. Mol. Struct.*, 2023, **1278**, 134849.
22 A. Jebli, A. E. Amri, R. Hsissou, A. Lebkiri, B. Zarrik, F. Z. Bouhassane, E. mahdi Hbaiz, E. H. Rifi and A. Lebkiri, *J. Taiwan Inst. Chem. Eng.*, 2023, **149**, 105006.
23 S. Yasmin, M. H. Kabir, N. Roy and S. Jeon, *ECS Adv.*, 2023, **2**, 024504.
24 A. El Amri, R. Hsisou, A. Jebli, I. Lebkiri, J. Bensalah, F. Z. Bouhassane, L. Alami, A. Lebkiri, A. Zarrouk, E. H. Rifi and A. Lebkiri, *Chem. Afr.*, 2024, **7**, 345–365.
25 M. Xiao, X. Zhang, X. Liu, Z. Chen, X. Tai and X. Wang, *ACS Macro Lett.*, 2025, **14**, 1201–1220.
26 Md. Yeasin Pabel, S. Yasmin, M. A. A. Shaikh and M. H. Kabir, *Sensor Actuator Phys.*, 2024, **366**, 115028.
27 K. S. Pasupuleti, A. M. Thomas, D. Vidyasagar, V. N. Rao, S.-G. Yoon, Y.-H. Kim, S.-G. Kim and M.-D. Kim, *ACS Mater. Lett.*, 2023, **5**, 2739–2746.
28 X. Pan, J. Ji, N. Zhang and M. Xing, *Chin. Chem. Lett.*, 2020, **31**, 1462–1473.
29 M.-L. Cui, Z.-X. Lin, Q.-F. Xie, X.-Y. Zhang, B.-Q. Wang, M.-L. Huang and D.-P. Yang, *Food Chem.*, 2023, **412**, 135554.
30 Md. G. Azam, M. H. Kabir, Md. A. A. Shaikh, S. Ahmed, M. Mahmud and S. Yasmin, *J. Water Proc. Eng.*, 2022, **46**, 102597.
31 M. H. Kabir, M. J. Miah, A. K. Mohiuddin, Md. S. Hossain, B. P. Upoma, M. A. A. Shaikh, M. Y. Pabel, F. Mojumder, R. Mahmud, N. I. Tanvir and S. Yasmin, *ACS Sustainable Resour. Manage.*, 2025, **2**, 256–266.
32 S. Yasmin, M. G. Azam, M. S. Hossain, U. S. Akhtar and M. H. Kabir, *Heliyon*, 2024, **10**(12), DOI: 10.1016/j.heliyon.2024.e33317.
33 B. P. Upoma, S. Yasmin, Md. A. Ali Shaikh, T. Jahan, Md. A. Haque, M. Moniruzzaman and M. H. Kabir, *ACS Omega*, 2022, **7**, 29655–29665.
34 S. Yasmin, S. Cho and S. Jeon, *Appl. Surf. Sci.*, 2018, **434**, 905–912.
35 A. K. Mohiuddin, S. Yasmin and S. Jeon, *Sensor Actuator Phys.*, 2023, **355**, 114314.
36 S. Yasmin, M. S. Ahmed and S. Jeon, *J. Nanosci. Nanotechnol.*, 2017, **17**, 3959–3966.
37 F. Monehzadeh and Z. Rafiee, *Appl. Organomet. Chem.*, 2020, **34**, e5631.
38 S. M. Badawy, *Environ. Prog. Sustainable Energy*, 2016, **35**, 1485–1491.
39 M. Sakil, M. H. Kabir, Md. A. Jabbar, Md. S. Hossain, A. M. Kusum, T. Jahan, M. Shahriar Bashar and S. Yasmin, *ACS Appl. Nano Mater.*, 2025, **8**, 22722–22735.
40 Md. H. Kabir, Md. S. Hossain, M. M. Rahman, Md. Ashrafuzzaman, M. Hasan, Md. Y. Pabel, D. Islam, M. Shahriar Bashar, T. Faruque and S. Yasmin, *ACS Sustainable Resour. Manage.*, 2024, **1**, 1812–1823.
41 N. Roy, S. Yasmin and S. Jeon, *Microchem. J.*, 2020, **153**, 104501.
42 M. SefidSiahbandi, O. Moradi, B. Akbari adergani, P. A. Azar and M. S. Tehrani, *Chemosphere*, 2023, **312**, 137184.
43 N. Borane, R. Boddula, N. Odedara, J. Singh, M. Andhe and R. Patel, *Nano-Struct. Nano-Objects*, 2024, **39**, 101282.
44 C. O. Aniagor, C. A. Igwegbe, J. O. Ighalo and S. N. Oba, *J. Mol. Liq.*, 2021, **334**, 116124.
45 O. Saha, M. Humayun Kabir, M. Mazharul Islam, M. Sanwar Hossain, M. Shahriar Bashar, M. Yeasin Pabel and S. Yasmin, *RSC Adv.*, 2025, **15**, 41874–41885.

46 S. Datta, M. H. Kabir, M. S. Rahman, M. Y. Pabel, T. Jahan, T. Sharmin and S. Yasmin, *RSC Adv.*, 2025, **15**, 48923–48936.
47 M. S. Hossain, M. H. Kabir, M. A. Ali Shaikh, M. A. Haque and S. Yasmin, *RSC Adv.*, 2024, **14**, 1431–1444.
48 E. N. Bakatula, D. Richard, C. M. Neculita and G. J. Zagury, *Environ. Sci. Pollut. Res.*, 2018, **25**, 7823–7833.
49 S. Islam, M. H. Kabir, T. Jahan, U. S. Akhtar and S. Yasmin, *Sensor Actuator Phys.*, 2025, **393**, 116791.
50 Md. S. Hossain, S. Yasmin and M. H. Kabir, *J. Saudi Chem. Soc.*, 2024, **28**, 101873.
51 S. Guo, G. Zhang, Y. Guo and J. C. Yu, *Carbon*, 2013, **60**, 437–444.
52 S. F. Shaikh, R. S. Mane, B. K. Min, Y. J. Hwang and O. Joo, *Sci. Rep.*, 2016, **6**, 20103.
53 F. Mojumder, S. Yasmin, M. A. A. Shaikh, P. Chowdhury and M. H. Kabir, *J. Hazard. Mater. Adv.*, 2024, **14**, 100429.
54 M. Y. Pabel, M. H. Kabir and S. Yasmin, *J. Energy Storage*, 2025, **119**, 116314.
55 X. Li, L. Ai and J. Jiang, *Chem. Eng. J.*, 2016, **288**, 789–797.
56 K. H. Shah, M. Fareed, M. Waseem, S. Shahida, M. R. Hatshan, S. Sarfraz, A. Batool, M. Fahad, T. Ahmad, N. S. Shah, K. Ha and C. Han, *Water*, 2023, **15**, 3541.
57 R. Wahab, F. Khan and A. A. Al-Khedhairy, *RSC Adv.*, 2018, **8**, 24750–24759.
58 D. Chen, A. E. Martell, R. J. Motekaitis, S. Niu and D. McManus, *Inorg. Chim. Acta*, 1999, **293**, 206–209.
59 Md. S. Hossain, S. Yasmin, N. T. Dipannita, Md. S. Hossain, S. C. Sarker, T. Jahan, Md. A. Kabir, R. K. Paul and M. H. Kabir, *Clean. Chem. Eng.*, 2025, **12**, 100214.
60 J. Korać Jačić, M. Dimitrijević, D. Bajuk-Bogdanović, D. Stanković, S. Savić, I. Spasojević and M. R. Milenković, *J. Biol. Inorg. Chem.*, 2023, **28**, 679–687.
61 Y. Chao, W. Zhu, X. Wu, F. Hou, S. Xun, P. Wu, H. Ji, H. Xu and H. Li, *Chem. Eng. J.*, 2014, **243**, 60–67.
62 S. Liu, Y. Liu, X. Tan, S. Liu, M. Li, N. Liu, Z. Yin, S. Tian and Y. Zhou, *J. Chem. Technol. Biotechnol.*, 2019, **94**, 2187–2197.
63 Y. Wang, Q. Geng, J. Yang, Y. Liu and C. Liu, *ACS Omega*, 2020, **5**, 31137–31145.
64 N. Tabassum Dipannita, S. Yasmin, M. Kamrul Hasan, M. Sanwar Hossain, M. Akter Somapti and M. Humayun Kabir, *RSC Adv.*, 2025, **15**, 35219–35232.
65 X. Pan, F. Kong and M. Xing, *Res. Chem. Intermed.*, 2022, **48**, 2837–2855.
66 R. F. Abbas, H. K. Hami and N. I. Mahdi, *Int. J. Environ. Sci. Technol.*, 2019, **16**, 5439–5446.
67 B. Bai, X. Xu, C. Li, J. Xing, H. Wang and Y. Suo, *J. Nanomater.*, 2018, **2018**, 1–14.
68 W. K. Abdulsahib, S. H. Ganduh, M. A. Mahdi and L. S. Jasim, *Int. J. Appl. Pharm.*, 2020, 100–106.
69 S. Zaidi, V. Sivasankar, T. Chaabane, V. Alonzo, K. Omine, R. Maachi, A. Darchen and M. Prabhakaran, *J. Environ. Chem. Eng.*, 2019, **7**, 102876.
70 G. Kaur, N. Singh, A. Rajor and R. K. Arya, *Environ. Sci. Pollut. Res.*, 2023, **30**, 8485–8499.
71 G. Kaur, N. Singh and A. Rajor, *ChemistrySelect*, 2021, **6**, 3139–3150.
72 A. M. Abdelfatah, N. El-Maghrabi, A. E. D. Mahmoud and M. Fawzy, *Sci. Rep.*, 2022, **12**, 19372.
73 R. Rostamian and H. Behnejad, *Environ. Sci. Pollut. Res.*, 2018, **25**, 2528–2537.